BACHELOR

Experimental study on the relation between material properties and printing parameters in SLS 3D printing

Leenaerts, Luuk A.

Award date:
2023

Eindhoven University of Technology

Department of Mechanical Engineering

Bachelor end project
Q1-Q2 2022-2023

Experimental study on the relation between material properties and printing parameters in SLS 3D printing

Author
Leenaerts, L.A.
1363069

Supervisors
dr. ir. Van Breemen, L.C.A.
ir. Van Berlo, F.P.A

Eindhoven, January 25, 2023

Contents

1 Introduction

Selective laser sintering (SLS) 3D printing is an additive manufacturing technique that uses a high-power CO_2 laser to sinter powder particles together to form a desired 3D-printed object. Compared to various other additive manufacturing techniques, SLS has several advantages, including multiple machine retailers and a wide scale of available metals and plastics [Starr et al., 2011]. Currently, polyamide 12 (PA12) is the most used polymer-powder in 3D SLS printing. This semi-crystalline polymer has a relatively large sintering window as compared to other semi-crystalline polymer, of approximately 25 °C as shown in Figure 1 [Schmid, 2018].

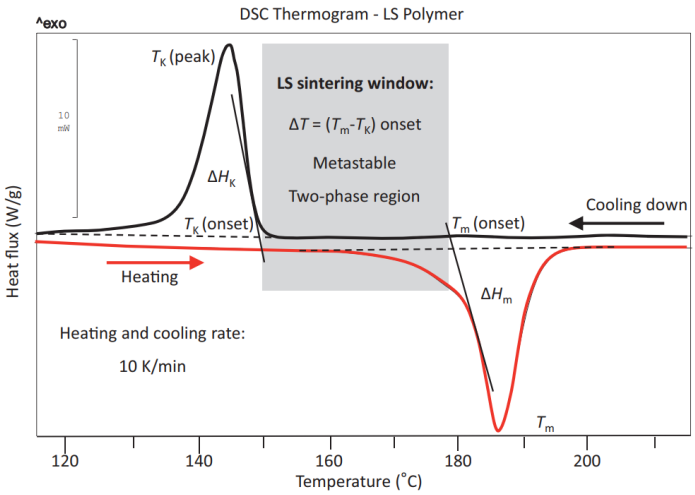

Figure 1: DSC measurement of PA12 performed at a heating and cooling rate of 10 K/min. The sintering window is shown between the onset melting temperature (T_m (onset)) and the onset crystallization temperature (T_k (onset)) (Schmid, 2018).

The key of making high-quality parts in SLS printing is the control of the printing parameters, for example laser power, layer thickness and bed temperature. In literature, a wide range of studies has been performed that show the dependency of part quality on printing settings [Starr et al., 2011]. A first relation to describe printing quality based on printing parameters is derived in a study by Nelson et al., 1993. In a later study, [Nelson et al., 1995], have showed that combinations of three processing parameters: laser power, P, laser scan speed, v, and laser beam spacing, y, can be used to estimate the area energy density:

$$E_D = \frac{P}{vy}. \tag{1}$$

In addition, the layer thickness h of the powder can be included for the relation for the volume energy density, as in for example the work of [Drummer et al., 2010]:

$$E_V = \frac{P}{vyh}. \tag{2}$$

However, herein it is assumed that the volume that is irradiated by the laser is proportional to the layer thickness. However, this volume is also dependent on the beam shape and more importantly the penetration depth (i.e. absorption coefficient) of the laser. This penetration depth should exceed the powder layer thickness for good sintering and adhesion. Therefore, it is concluded that the relation for the volumetric energy density is not an improvement on

the energy density relation [Schmid, 2018]. In the work of Bourell et al., 2014, it is found that controlling the bed temperature is crucial, because this effects porosity and mechanical properties. Also, the bed temperature has to be within the sintering region. Preferably, the bed temperature should be chosen close to the melting peak to avoid premature and uncontrolled crystallization processes which can cause for example warpage [Schmid, 2018]. A relation which includes additional print parameters is introduced by Starr et al., 2011, with the relation for the energy-melt-ratio (EMR). EMR is a more extensive and practical method to compare different LS parameters, since it includes the bed temperature. EMR shows a ratio between the applied energy provided by the laser divided by the energy needed for melting of a single layer of the used material [Vasquez et al., 2013]:

$$EMR = \frac{E_V}{E_M} = \frac{P/(yvh)}{(c_p(T_m - T_b) + \Delta H)\rho\Phi,} \tag{3}$$

where E_V, E_M, c_p, T_m, T_b, $\triangle H_m$, ρ, Φ are volume energy density, energy to melt, specific heat capacity, onset melting temperature, bed temperature, heat of fusion, material density, and packing density, respectively. EMR has shown to be an useful method to describe the relation between print parameters and the physics of powder melting. It was found in the studies by Vasquez et al., 2013 and Starr et al., 2011, that an increase in the EMR results in a rising powder sintering temperature, which in its turn results in mechanical properties to increase. Here, the Young's modulus, elongation at break and yield stress have all shown to reach increasingly higher values once the EMR is increased. The yield stress of prints however did show in the study by Vasquez et al., 2013 and Starr et al., 2011 to become constant at a high EMR as shown in Figure 2. The same trend was found in the study by Vasquez et al., 2013 and Starr et al., 2011 for the Young's modulus.

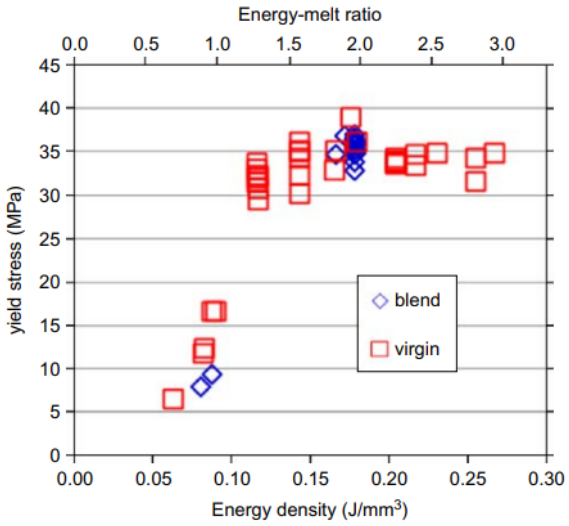

Figure 2: Relation between energy-melt-ratio, yield stress and energy density. A steep increase for the yield stress is seen up to approximately 0.12 J/mm^3 until the yield stress remains approximately constant at higher EMR [Starr et al., 2011].

In a study by Bierwish et al., 2021 a variation on the EMR, called the attenuation melt ratio (AMR), was introduced. This relation can be seen in Equation 4. This study takes a closer look at degradation and also includes attenuation [Bierwisch et al., 2021].

$$\text{AMR} = h\Phi a(1-R)\text{EMR} \tag{4}$$

where a and R are the absorption coefficient in units of reciprocal length and the reflection coefficient, respectively.
In previous work, an extension to a table-sized commercial SLS printer was developed to incorporate temperature control with an IR camera [Van Haren, 2022]. This enables us to study the influence of bed temperature on printing quality. Therefore, a simplified version of the EMR ratio, the EMR*, is introduced with two adjustable printing parameters: the laser power and the bed temperature:

$$\text{EMR}^* = \frac{P}{c_p(T_m - T_b) + \triangle H_m}. \tag{5}$$

In this study, experiments are performed to study the effect of laser power and bed temperature on printing quality. Instead of optimizing printing parameters, we are interested in the relation of part quality with respect to EMR (or EMR*). Other studies, as for example the study by [Starr et al., 2011], studied the relation between the EMR and mechanical properties. However, here the bed temperature was not varied. One of the research goals is to investigate if a constant EMR will result in the same part quality. In this study the focus also lies on finding out whether the EMR*, including the bed temperature as a variable print parameter, is applicable at all, since it is very hard to control the bed temperature in most printing processes. In Chapter 2 the used materials and methods in this study are elaborated. Subsequently, the results and discussions are given in Chapter 3. The conclusions and recommendations are given in Chapter 4. Finally, an outlook is given to elaborate on following steps in this research.

2 Materials and methods

2.1 Material properties

The polymer powder which is used is a PA12 grade from EOS (PA2200). The density of the used PA12 is 930 kg/m^3 and the molecular weight is 15000 g/mol [EOS GmbH, 2019]. A 100% virgin batch of powder is used for printing. No thermal treatment is applied and no powder is reused or mixed. All the powder is sieved beforehand to ensure that no lumps of powder enter the printer and end up in the powder bed.
To determine the melting and crystallization processes of the PA2200, multiple DSC measurements are executed. From this data the onset melting temperature and heat of fusion, used to calculate the EMR*, were obtained. From the DSC data the sintering window of the PA2200 could also be determined. To study the influence of ageing and differences in powders produced by different suppliers, more DSC measurements were executed, these results can be found in Appendix A.1.

2.2 Printer properties

The SLS printer used in this study is the SnowWhite printer manufactured by ShareBot. The SnowWhite is equipped with a 14 W CO_2 laser with a spot size diameter of 200 μm. In this study an one layer print in the shape of a hexagon is used for all tests. The hexagon print, including dimensions in mm, can be seen in Figure 3. Using a hexagon shape and printing just a single layer, ensures that prints can easily be assessed on warpage and porosity. Moreover, multiple tensile bars can be extracted from a single hexagon print.
Some of the adjustable print parameters are not varied during printing and kept constant, these fixed parameters can be found in Table 1. The laser power can only be adjusted in percentages and not in watt. To convert between the laser power in percent (P_p) and the laser power in watt (P) we use: $P = -3.6003 + 0.3504P_p$ [Bastiaansen, 2019]. To convert the laser speed from point/s (v_p) to mm/s (v) we can use: $v = 0.046875v_p$ [Bastiaansen, 2019]. The border power, which is the laser power for the border of the object, is kept constant at 3.4 W. The waiting time is the number of seconds to wait at the end of the heating process and before starting the printing process. The warming layers are the number of pre-heating layers which must be done before starting the printing process and the environmental temperature is the temperature at which the build chamber is kept constant.

Table 1: Fixed parameters used in the Sharebot Snowwhite 3D printer.

Parameter	**Value**	**Unit**
Laser speed	1875 (40000)	mm/s (points/s)
Border laser speed	1875 (40000)	mm/s (points/s)
Powder layer	800	μm
Layer thickness	200	μm
Border power	3.4 (20)	W (%)
Waiting time	1200	s
Hatching space	100	μm
Warming layers	20	-
Env. Temperature	155	°C

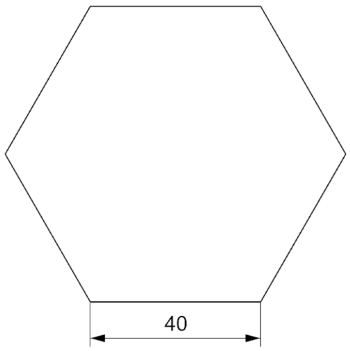

Figure 3: Hexagon shape with a thickness of 0.2 mm.

To control the bed temperature an Optris 640PI IR camera (with a 33° lens with IR filter for the CO_2 laser light) is built into the printer, such that the bed temperature can be controlled using remote software [Van Haren, 2022]. Optris PIX Connect is used as a software tool to measure the bed temperature in specified areas [Optris, 2023], by means of an Arduino Mega this data is then sent to the printer. By means of the IR camera the bed temperature can be controlled to a chosen temperature with an accuracy of 4 °C. The bed temperature is controlled to the maximum temperature measured in the measurement area. The used measurement area can be seen in the example of the control window in Figure 4. The emissivity settings of the IR camera are used for calibration. This calibration has been performed before each print, to ensure accurate temperature control. The heating lamps inside of the printer have been replaced, such that the powder bed is heated more homogeneously. Herefore, the two 230 W halogen lamps placed above powder bed have been replaced by two 150 W halogen lamps. Furthermore, the 120 W halogen lamp positioned at the door has been replaced by a 300 W halogen lamp. At last, to ensure the environmental temperature could not impact the bed temperature control, the printer is heated up for at least two hours before any prints were performed.

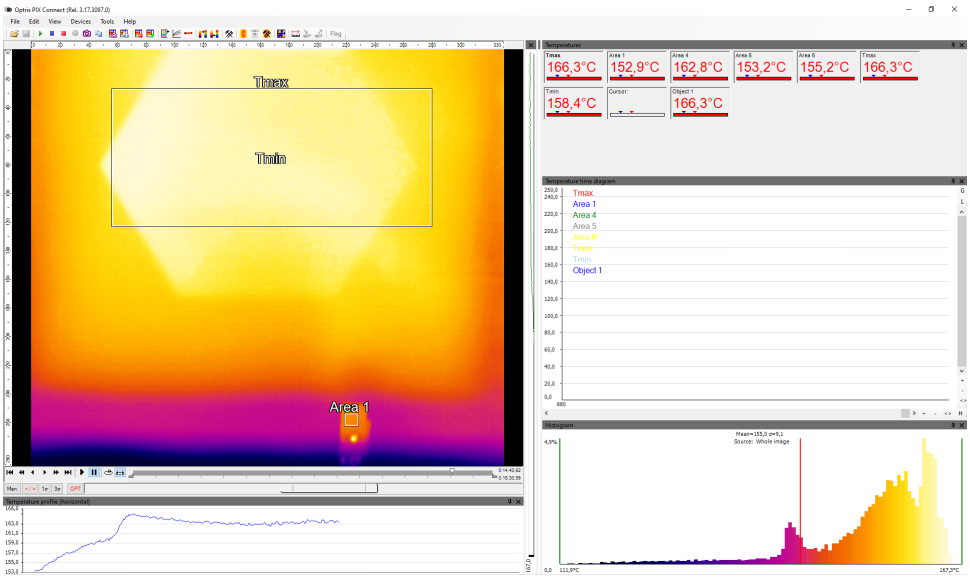

Figure 4: Optrix PIX connect temperature control window, after a hexagon has been printed, used to control bed temperature. The grey rectangle represents the measurement area.

2.3 Print assessment methods

A ZwickRoell tensile tester with a 100 N load cell is used for mechanical testing [ZwickRoell, 2023]. Tensile bars with a neck width of 1.5 mm are used as shown in Figure 5. The tests were performed at a strain rate of 0.001 s^{-1} and at room temperature. From each printed hexagon, samples were obtained from different positions, as shown in Figure 6. Here a distinction is made in samples located on the outside and inside of the hexagon print. The samples positioned on all far six sides of the hexagon are labelled to be positioned on the outside, all other samples are labelled to be positioned on the inside of the print.

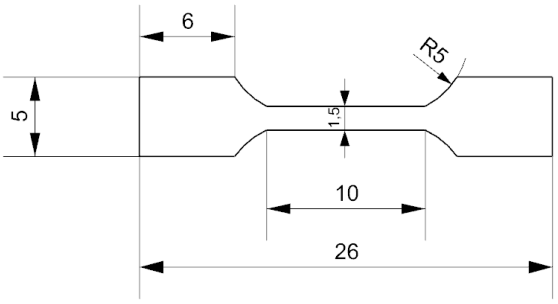

Figure 5: Tensile bar sample with dimensions in mm.

Besides tests by means of the tensile tester, also the density of all samples and visual inaccuracies, such as warpage, are assessed. To determine the density, all samples used in the tensile tests are weighted beforehand. By means of the mass and volume of the samples, the density can be determined and evaluated for different values for the EMR*. To assess visual inaccuracies, photographs of all prints are taken and evaluated. To assess warpage of the printed hexagons, the height w shown in Figure 7 has been taken as measurement criterion.

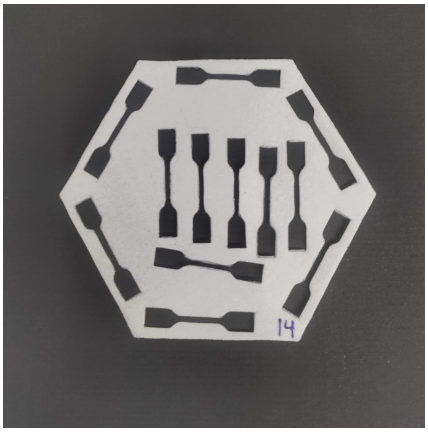

Figure 6: Positioning samples in printed hexagons.

Figure 7: Height taken as measurement criterion for warpage.

3 Results and discussion

To study the relation between the EMR* and material properties, multiple parameter sets have to be found to be able to print for a constant EMR*. Herefore one must take into account the limitations of the adjustable parameters used in the EMR*. Multiple prints were manufactured, where the laser power and bed temperature were varied to find the limitations these parameters and thus the EMR* relation itself hold. All prints which were not usable for testing or were not able to be manufactured at all, are visualised with a cross in Figure 8. Here the y-axis is the energy to melt (E_M) and the x-axis is the laser power (P). All prints which were successfully manufactured are visualised with a circle in Figure 8. EMR* is calculated from Equation 5, where $c_p = 2350$ J/kg [EOS GmbH, 2019], $\Delta H = 110.78$ J/kg, and $T_m = 180$ °C are used. The heat of fusion and melting temperature are extracted from the DSC measurements on virgin PA2200 (see Appendix A.1).

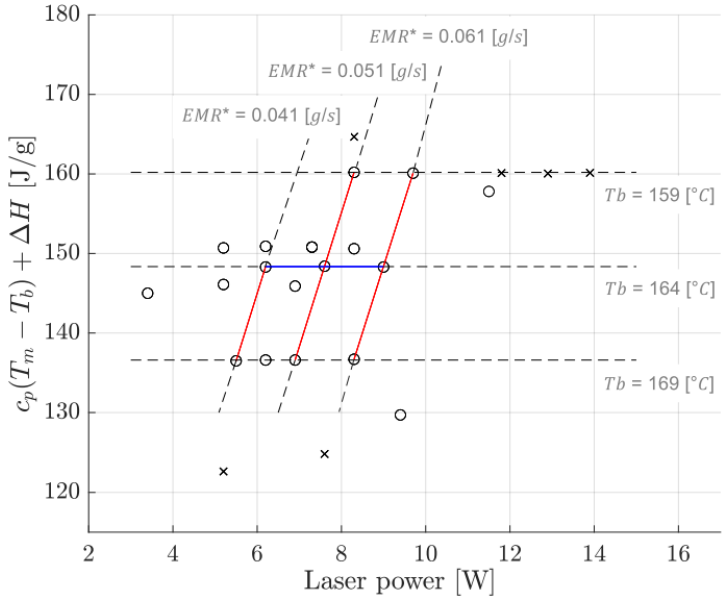

Figure 8: Measurements points for different laser power and bed temperature combinations. The red lines show a parameter set for a constant EMR* and the horizontal blue line shows a parameter set for an increasing EMR* and constant bed temperature of 164 °C. Circles and crosses visualise successfully and not successfully printed hexagons, respectively.

3.1 Print parameter limitations

The first set of failed prints have an energy of melting below 125 J/g (see Figure 8). This corresponds with a temperature of larger than 173 °C. At these set bed temperatures the powder bed already began to partially melt before the powder-bed was exposed to energy provided by the laser. Figure 9 shows a powder bed at a controlled temperature of 172 °C, where the temperature in the bed is not homogeneous and small areas of particles have prematurely melted together. This can cause the powder bed to clot together and disrupt the spreading of powder during or before printing. Even when a manufactured print is printed successfully after this occurrence, the mechanical properties of the print will not be homogeneous throughout the printed object. Although a bed temperature of 172 °C would be printable according to the sintering window of the used PA2200, there are some reasons why this did not work in this printer. First of all, the bed temperature is controlled with an accuracy of 4 °C. Actual temperatures in the printer will therefore vary from the controlled set bed temperature. Besides, the bed temperature is only controlled in a specific measurement area on the powder bed, as shown in Figure 9, but

not on the powder tanks positioned next to the powder bed. If the uncontrolled temperature of the powder, provided by the powder tanks, heats up at higher rates than the powder bed this will lead to premature melting at the powder tanks. If the powder on top of the powder tanks already starts to partially melt, this can cause the powder bed to clot together when the recoater passes over the powder bed.
Looking at the DSC data, the onset melting temperature of the used PA12 is around 180 °C. Given this fact, a bed temperature of for example 174 °C should theoretically not form any problem for printing. However, a DSC measurement shows an idealised measurement curve that works with relatively high and linear heating and cooling rates. However in the SLS reality, there are nonlinear and uncontrollable temperature change rates [Schmid, 2018]. Therefore, it is up for debate whether the used onset melting temperature is accurate.

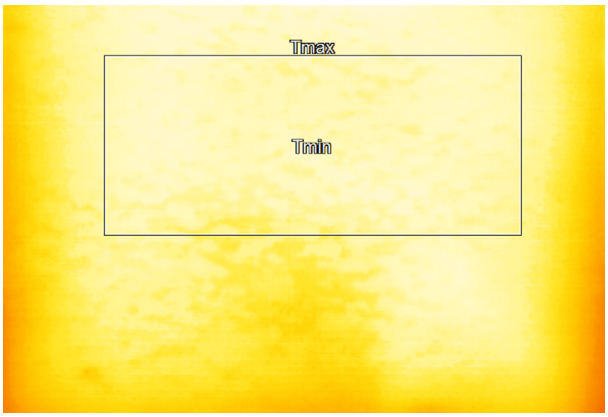

Figure 9: Inhomogeneous temperature distribution on controlled powder bed at set bed temperature of 172 °C. Maximum temperature difference in the measurement area is 6 °C.

A second limitation on the print parameters, used in the EMR*, occurs at bed temperatures close to the onset crystallization point. At an energy of melting of 160 J/g and higher (see Figure 8), premature and uncontrolled crystallization occurs. This corresponds with temperatures of 159 °C and lower. As a result, the parts show severe warpage during printing and often the printed object would be wiped off the powder bed by the recoater. As a result of these limitations, the sintering window has been reduced from 25 °C, as shown in DSC, to only 10 °C in the printer.
Besides limitations regarding the set bed temperature, printing is limited by the laser power, as can be seen in Figure 8. Multiple measurements were done at an energy of melting of 160 J/g (i.e. $T_b = 159$ °C) in combination with an increasing value for the laser power. Here, the laser power is limited due to warpage, which for example can be seen in the hexagons printed at a laser power of 11.80 W and a set bed temperature of 159 °C shown in Figure 10. By means of an increasing laser power, more energy is stored at the surface of the object. At these laser powers, powder particles fuse together to produce more dense parts, leading to a decrease in porosity and volume. Moreover, during heating, the part expands due to the coefficient of thermal expansion. Since the temperature is constantly changing within the part, a temperature gradient is forming from the bottom of the part to the top and also from the centre to the edges of the part. The resulting thermal expansion causes internal stresses and thus warpage. Note that we used a large flat surface susceptible to warpage. In case of smaller aspect ratios, these laser powers might be acceptable. A deformation of one of the corners of the printed hexagon would often cause the recoater to either fold the printed part or drag the part of the powder bed entirely.

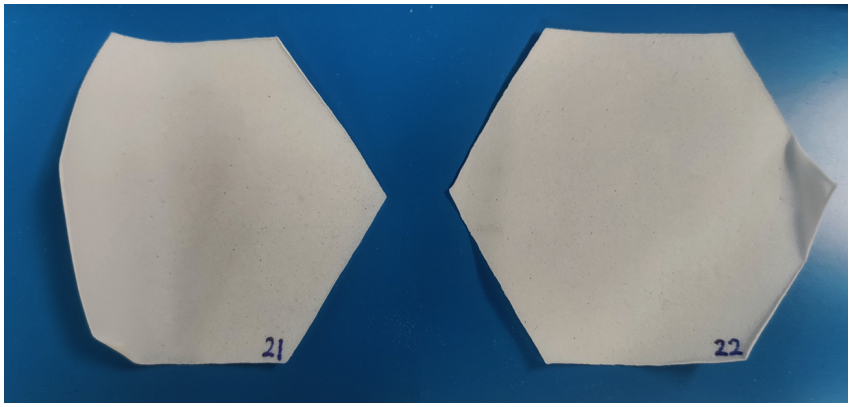

Figure 10: Warpage due to internal stresses resulting from extensive laser power for two samples printed at 159 °C and 11.8 W.

3.2 Tensile testing of printed parts

Within the given limitations for the laser power and bed temperature, multiple prints were produced using the parameter sets shown in Table 2. All printed parts can be found in Appendix A.2.

Table 2: Parameter sets where the laser power and bed temperature are varied, which result in different EMR* values.

Print number	**27**	**28**	**24**	**25**	**26**	**14**	**15**	**16**	**17**	**18**
P [W]	6.20	5.50	8.30	7.60	6.90	9.70	9.00	8.30	9.40	11.50
T_b [°C]	164	169	159	164	169	159	164	169	172	160
EMR* [g/s]	0.042	0.040	0.052	0.051	0.051	0.061	0.061	0.061	0.073	0.073

The parameter sets are chosen to show multiple relations. First of all measurements were performed at constant EMR* (print combination 14/15/16, 24/25/26, 27/28 and 17/18). Three constant EMR* values: 0.041, 0.051 and 0.061, are indicated in Figure 8 by the three red lines (from left to right). For a different combination of parameter sets (print combination 16/26/28, 15/25/27 and 14/24) a constant energy of melting is used. Here, the bed temperature is constant in each set and laser power is varied, resulting in a non-constant EMR* in each set. One of these sets, print combination 15/25/27, is indicated by the blue line in Figure 8.

Tensile test results, for all prints given in Table 2, can be seen in Figure 11 to 17. Herein, the tensile properties are shown in relation to the EMR* and bed temperature with error bars representing the one time standard deviation of the results. Figure 11 shows the typical stress strain curves for all prints. From the data obtained from the stress strain curves, the Young's modulus, ultimate tensile strength and elongation at break were assessed.

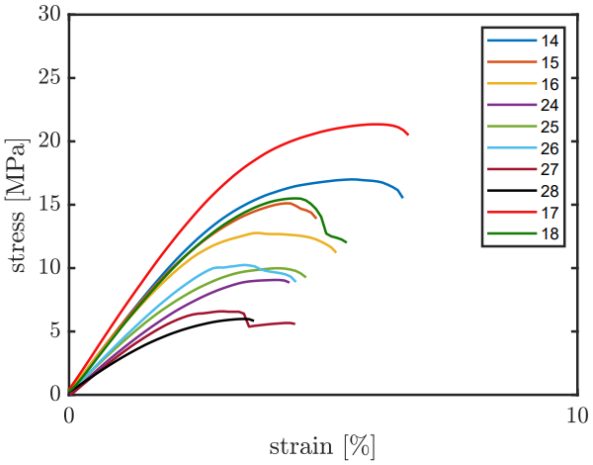

Figure 11: Typical stress strain curves for print parameter sets as given in Table 2.

Figure 12 shows a clear trend between the Young's modulus and the EMR*. Here, a higher value for the EMR* results in a higher Young's modulus. This can be explained by the relatively high level of energy which is put into the system by the laser power, which in its turn will result in a progressive increase in the powder sintering temperature. A constant value for the EMR* results in approximately similar Young's moduli. Therefore, for single layer prints it can be concluded that the EMR* is a good measure for the quality of printing in terms of the Young's modulus. Figure 13 shows that the elongation at break shows approximately the same relation with the EMR*, as shown for the Young's modulus. An increasing value for the EMR* results in an increasing elongation at break. In Figure 14 the ultimate tensile strength as a function of the EMR* is shown. From this figure, it follows that the EMR* might not be suitable for predicting the ultimate tensile strength. This is because for the first two parameter sets of EMR*'s a near constant ultimate tensile strength is measured. Only the two largest values of EMR* shows an increase in ultimate tensile strength. However, the spread on this data is quite large as compared to the Young's modulus and elongation at break. More data is required to draw conclusions for the ultimate tensile strength.

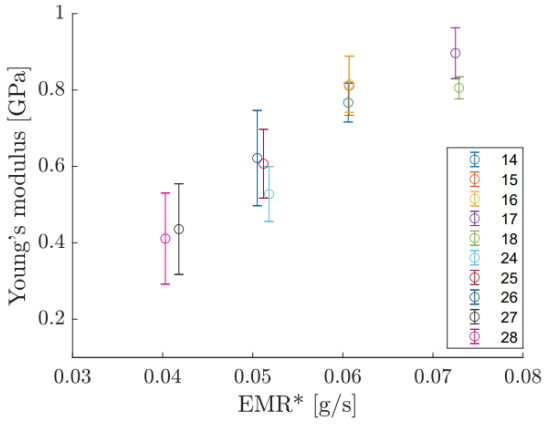

Figure 12: Relation between the Young's modulus and the EMR* for all prints.

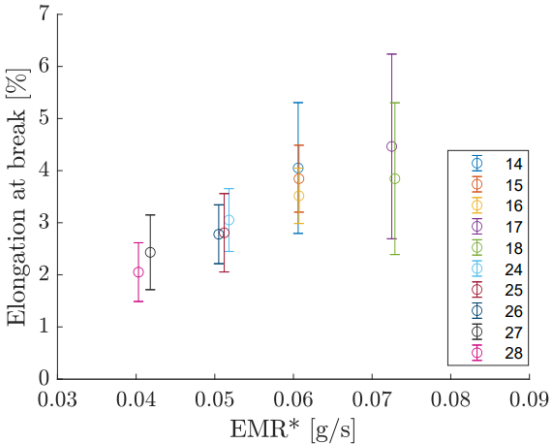

Figure 13: Relation between the elongation at break and the EMR* for all prints.

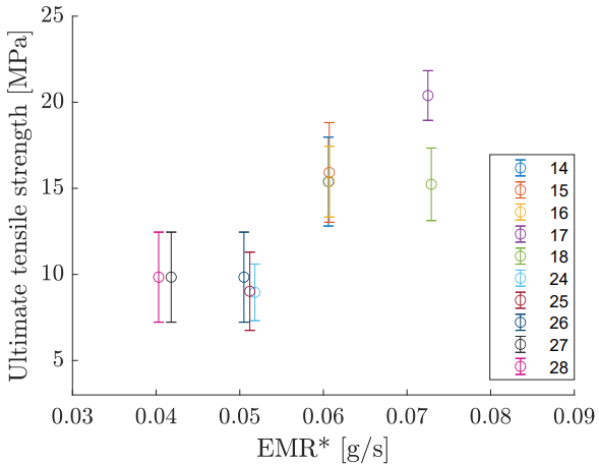

Figure 14: Relation between the ultimate tensile strength and the EMR* for all prints.

To evaluate if the change in mechanical properties is really an effect of changing the EMR* and not just the change in bed temperature, also the tensile properties are evaluated with respect to bed temperature. This can be seen in Figure 15 to 17. In Figure 15 it is shown that a difference in bed temperature does not significantly impact the Young's modulus for a constant value for the EMR*. A slight increase in mean Young's modulus for an EMR* of 0.07 g/s, 0.06 g/s and 0.05 g/s is visible. However, no clear conclusions can be obtained from this result. The bed temperature control accuracy of 4 °C might explain the only small difference shown in Figure 15, since the chosen parameter set uses bed temperatures with a step size of only 5 °C. Different from the Young's modulus, it looks like an increase in bed temperature results in a slightly smaller elongation at break, see Figure 16. However, no conclusions can be made since the results hold a large error margin, and furthermore print 17 does not follow this trend. In Figure 17 it can be seen that the bed temperature does not influence the ultimate tensile strength. Small deviations can be seen, but no real conclusions can be obtained from the results.
From these results it can thus be concluded that the combination of energy of melting and power (i.e. EMR*) are the determining parameters for tensile properties and not just the bed temperature.

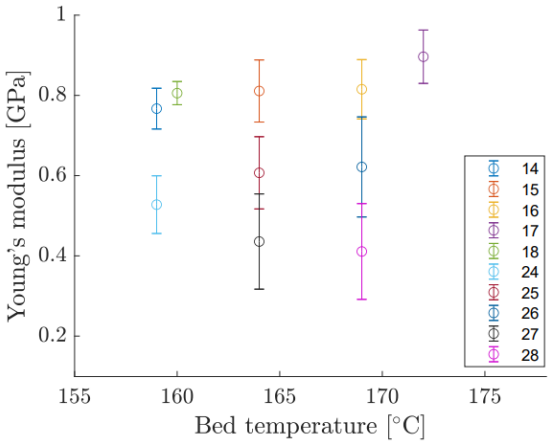

Figure 15: Relation between Young's modulus and the bed temperature for all prints.

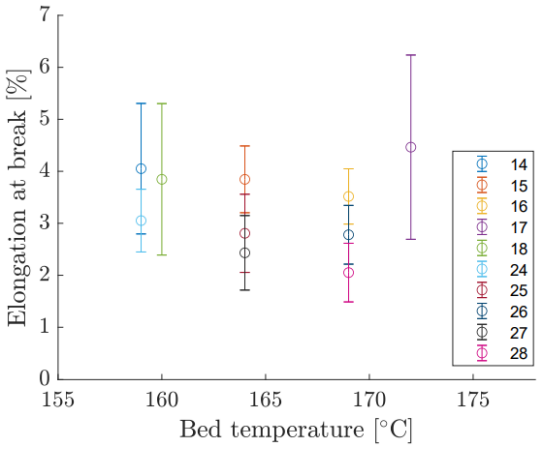

Figure 16: Relation between the elongation at break and the bed temperature for all prints.

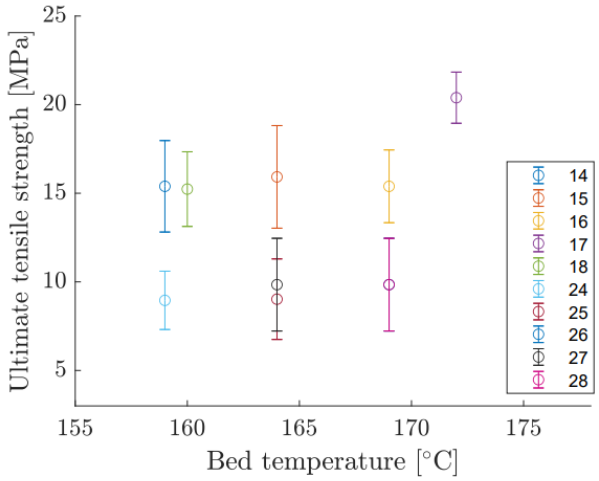

Figure 17: Relation between the ultimate tensile strength and the bed temperature for all prints.

It was validated that the position of the tensile bar in the hexagon has no significant effect on the tensile properties. Tensile bars retrieved close to the edges of the hexagon show similar Young's moduli as compared to tensile bars retrieved from the centre of the hexagon (see Appendix A.4).

3.3 Bulk density and tensile properties

The relation between the EMR* and the bulk density of each tested sample is plotted in Figure 18. The results show a clear trend. It can be concluded that an increasing EMR* results in an increasing bulk density of the printed samples. This can be explained by the relatively high level of energy which is put into the system by the laser power, which in its turn will result in a progressive increase in the powder sintering temperature. Therefore more particles enter a molten state and parts with an increased bulk density are formed. A difference can be seen in the bulk density for the two prints printed at an EMR* of 0.07 g/s (see Figure 8). Print 17 has shown premature melting, as shown in Figure 9, which can cause the increased bulk density. In Figure 19 the relation between the bulk density and the set bed temperature is shown. It can be concluded that no real trends are visible here and the bed temperature has no real influence on the bulk density of the printed parts.

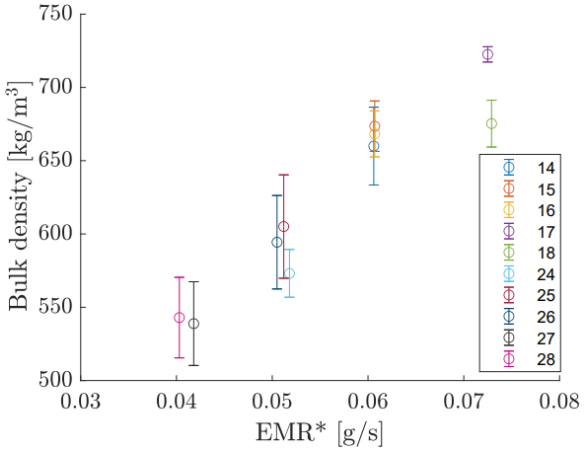

Figure 18: Relation between the bulk density and the EMR* of all prints.

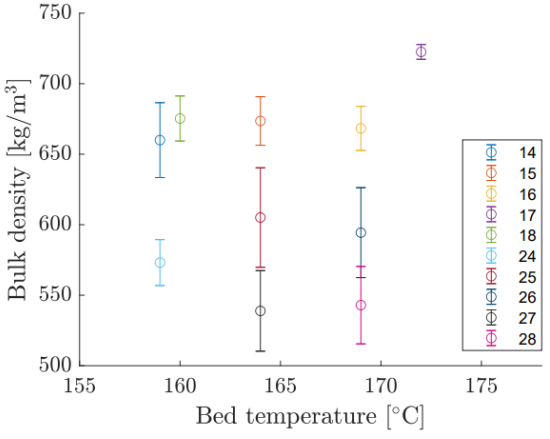

Figure 19: Relation between the bulk density and the bed temperature of all prints.

In Figure 20 to 22 the relation between tensile properties and the bulk density of the tested samples can be seen. A data-point for the Young's modulus, elongation at break and ultimate tensile strength with corresponding bulk density has been added to Figure 20 to 22 [EOS GmbH, 2019]. In Figure 20 a near linear relation can be seen between the bulk density and Young's modulus. The results show a trend approaching the given data-point. From this it can be concluded that the bulk density and Young's modulus for the single layer print correspond very closely with the data given by [EOS GmbH, 2019]. Figure 21 shows that an increasing value for the bulk density results in an increasing elongation at break. However in this case the relation does not show a trend approaching the given data point (see Figure 21). This result supports the non-linear relation found for the EMR* and elongation at break. For a bulk density of 600 kg/m^3 and higher a near linear relation can be seen with the ultimate tensile strength (see Figure 22). Here, similar as for the Young's modulus the ultimate tensile strength shows a trend approaching the given data-point by [EOS GmbH, 2019].

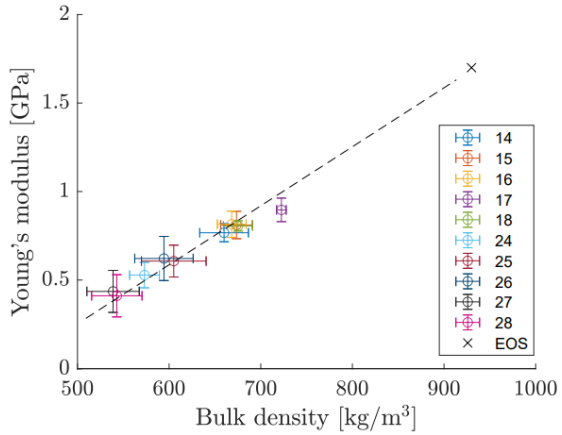

Figure 20: Relation between the bulk density and Young's modulus of all prints.

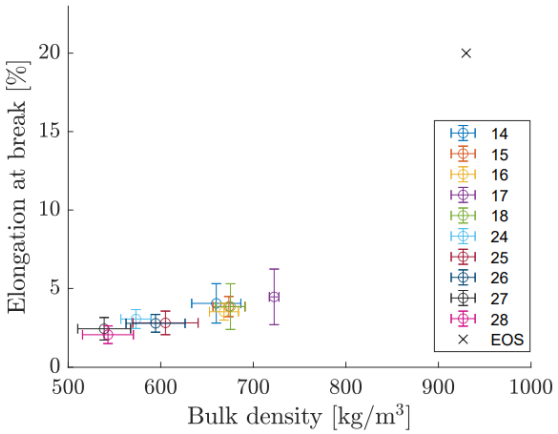

Figure 21: Relation between the bulk density and elongation at break of all prints.

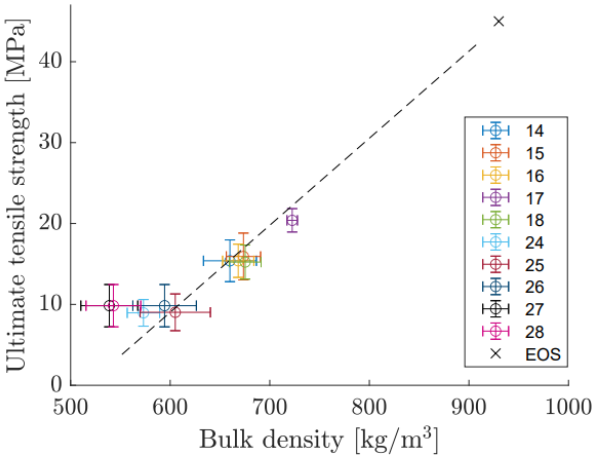

Figure 22: Relation between the bulk density and ultimate tensile strength of all prints.

3.4 Warpage

As mentioned in discussing the limitations of the print parameters, warpage can distort the printing process. Especially, for single layer prints with a relatively small layer thickness, similar as that of the printed hexagon in this study. In Figure 24 we see an example of one of the printed parts (print number 16) which shows warpage at the left edge of the hexagon. In Appendix A.3 supporting figures of warpage of all printed hexagons, as given in Table 2, are shown. In Figure 23 the impact of warpage has been visualised based on the height measurement criterion as introduced in Figure 7. Prints which exceeded the height limit of 3 mm were not usable for testing or were not able to manufactured at all due to excessive warpage, and are marked red. It can again be seen that once the limitations for the bed temperature are approached, warpage increases. It is therefore important to keep these limitations in mind when looking for an optimal print parameters set. Furthermore, a decrease in laser power in combination with a low bed temperature also results in relatively more warpage. This indicates that the EMR* is not a good criterion to predict warpage.

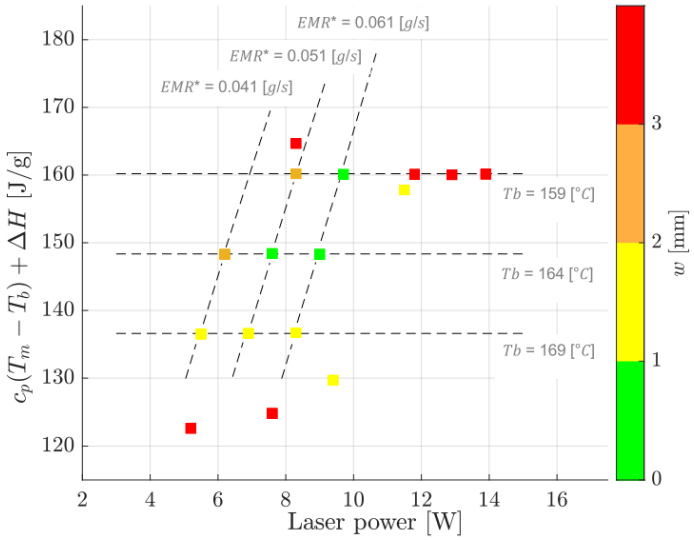

Figure 23: Height measurement criterion for warpage of manufactured prints.

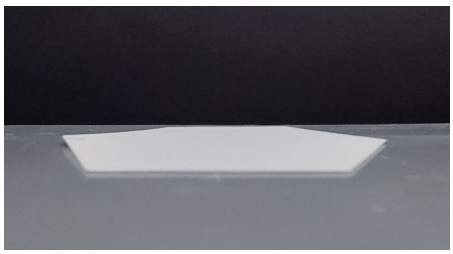

Figure 24: Warpage in print 16, printed with a laser power of 6.90 W and bed temperature of 169 °C.

3.5 Maximum temperature

The relation for the AMR (and EMR), is based on the ratio of energy input with respect to energy absorption resulting in melting. If this ratio is larger than one, full melting is expected. In the work of Bierwisch et al., 2021 it can be found that the maximum temperature at the surface can be calculated according to:

$$T_{\max} = \frac{aE_D(1-R)}{\rho c_p} - \frac{\Delta H}{c_p} + T_b. \tag{6}$$

With the use of the IR camera, the maximum temperature after irradiation with the laser is measured. The results are shown in Figure 25. Comparing this with the calculated maximum temperatures (Equation 6), using $a = 7790$ m^{-1}, R = 0.05 and $\rho = 925$ kg/m^3 [Balemans, 2019], an under prediction is found. The EMR* does not scale with the maximum temperature. The actual maximum temperature reached while sintering did in all cases reach a higher temperature than calculated via the relation by Bierwisch et al., 2021.

In Figure 26 the relation between the measured and theoretical maximum temperature, by [Bierwisch et al., 2021], is given. Here, a different set of constants used in Equation 6, obtained from [Li et al., 2020] and [Schuffenhauer et al., 2021], is compared against the constants used in the calculation for the maximum temperature given by [Balemans, 2019] and [EOS GmbH, 2019]. In Figure 26 the blue data points represent the constants from [Balemans, 2019] and [EOS GmbH, 2019], and the red data points from [Li et al., 2020] and [Schuffenhauer et al., 2021]. It is shown that with use of the red data set a closer approximation of the measured maximum temperature against the theoretical maximum temperature is given. The specific heat capacity given by [Li et al., 2020] is more accurate since all prints were manufactured close to the onset melting point and the specific heat capacity at these relatively high temperatures is higher than 2.35 $Jg^{-1}K^{-1}$, which is used in calculations for the EMR*. When the specific heat capacity is adjusted, the results for the EMR* relation will change as well. Further research could show whether an increase in specific heat capacity makes the EMR* relation more accurate to describe material properties.

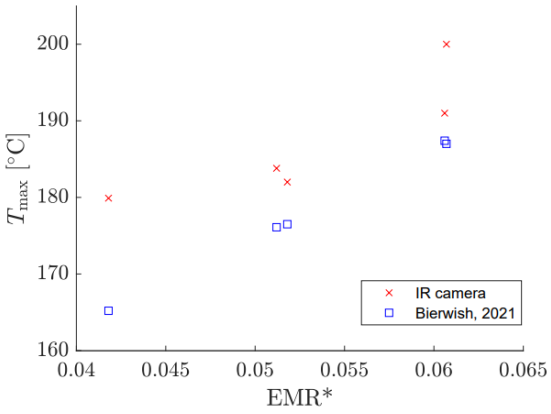

Figure 25: Relation between laser power and maximum temperature according to IR camera data and Bierwish et al.

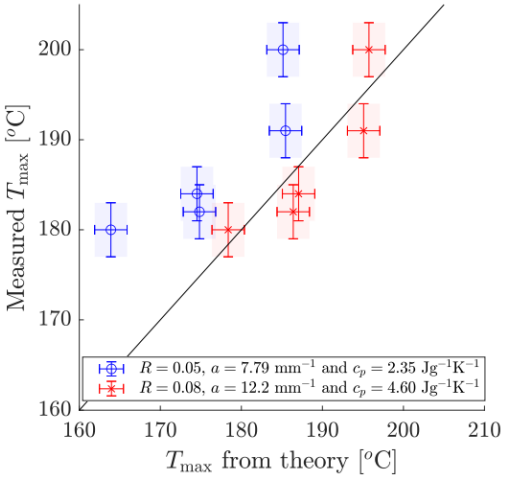

Figure 26: Relation between the measured and theoretical maximum temperature by Bierwish et al. The blue and red data points are plotted with a different constant set as shown in the legend.

An important concept that is not directly derivable from the energy ratio is the flow of material. For PA2200 it takes the order of seconds to sinter two particles together [Balemans, 2019]. With an increase of one order in viscosity of a particle, this time also increases at least one order. Since the viscosity of a molten polymer is related to temperature according to an Arrhenius type of relation [Verbelen et al., 2016], it can be argued that the maximum temperature plays an important role in the sintering process. IR camera data has shown that the maximum temperature is reached for only a fraction of a second. However, the time above melting does depend on the maximum temperature. I.e. the higher the maximum temperature, the longer a particle is in the molten state. So therefore, although this is not a direct measure, it is proposed to replace the energy of melting with the energy required to reach a set (maximum) temperature. The energy ratio including $T_{\max}$, the simplified energy-temperature-ratio (ETR*), is given by:

$$\mathrm{ETR}^* = \frac{P}{c_p(T_m - T_b) + \triangle H + c_p(T_{max} - T_m)}. \tag{7}$$

By means of ETR*, the maximum temperature is a measure for the viscosity and thus the sintering time. After rewriting, ETR* follows from:

$$\mathrm{ETR}^* = \frac{P}{c_p(T_b + T_{max}) + \triangle H}. \tag{8}$$

An increasing maximum temperature results in a shift of the crystallization peak for PA12, due to postcondensation reactions. This causes the print to reach the onset crystallization point relatively faster than prints manufactured at lower maximum temperatures [Verbelen et al., 2016]. This difference in onset crystallization point will result in a different micro structure, where prints manufactured at a higher set maximum temperature will have a micro structure with an increased spherulite size [Plummer et al., 2001]. While the Young's modulus increases with a growth of the crystals in the microstructure, properties such as elongation at break, impact strength, tensile strength, and yield stress might decrease [Schmid, 2018]. To prevent postcondensation reactions from impacting material properties, different materials can be used. Some other types of PA12, for example Orgasol, do not experience the postcondenstaion reactions seen for PA2200. Orgasol polyamide powder however does have a higher viscosity, which will require larger sintering times [Verbelen et al., 2016].

4 Conclusions and recommendations

In this study single layer hexagon parts are 3D printed and the quality of the prints are assessed on level of warpage, mechanical properties and bulk density. By varying the laser power and bed temperature, parts with constant and increasing energy-melt-ratios (EMR*'s) are produced in the SLS printer. Using tensile experiments, a near linear relation between the EMR* and Young's modulus is found. Results have shown that a constant EMR* can be used to manufacture prints with a near to constant Young's modulus. The results indicate that the energy-melt-ratio is a good parameter to assess the modulus of a part. Moreover, elongation at break shows to reach increasingly higher values once the EMR* is increased. The ultimate tensile strength is roughly the same for an EMR* of 0.041 g/s and 0.051 g/s. At an EMR* of 0.061 g/s and 0.073 g/s a significantly higher ultimate tensile strength was found. The impact of the bed temperature on tensile properties did not provide any clear relations. It can be concluded that the combination of energy of melting and power (i.e. EMR*) are the determining parameters for tensile properties. For warpage the bed temperature is the most important printing parameter. It was found that parts produced at bed temperatures close to the onset of crystallization and close to the onset of melting show significant warpage. Due to an error of about 4 °C in the control of the printer, a sintering window of only 10 °C was found. This emphasizes the importance of the temperature control in the SLS printer. Although bed temperature is the most important parameter for warpage, also internal stresses due to temperature gradients are a cause of warpage. It has been shown that this limits the maximum power that can be applied. EMR* is not able to describe this limit in power due to warpage.
Bulk density of printed parts has been measured and compared to the EMR* as well. A near linear relation between EMR* and the bulk density was found. By comparing the bulk density and tensile measurements, a clear linear relation between the Young's modulus and bulk density is found. The elongation at break shows approximately the same relation with the bulk density as shown in relation to the EMR*. An increasing value for the bulk density results in an increasing elongation at break. For a bulk density of 600 kg/m^3 and higher a near linear relation can be seen with the ultimate tensile strength. By extrapolation to the modulus and ultimate tensile strength of multi-layer printed dense parts it can be concluded that the found results with the bulk density and Young's modulus for a single layer print correspond very closely with the data given by [EOS GmbH, 2019]. At last a variation on the EMR*, the energy-temperature-ratio (ETR), has been introduced to find an even more accurate relation. The ETR takes into account the maximum temperature reached during manufacturing. The maximum temperature, obtained by the IR camera, reached while sintering did in all cases reach a higher temperature than calculated via the relation by [Bierwisch et al., 2021]. With use of different material constants given by [Li et al., 2020] and [Schuffenhauer et al., 2021] a better relation for the maximum temperature is described. Here, a higher specific heat capacity was used in calculations than used in the EMR*. Further research could show whether an increase in specific heat capacity makes the EMR* relation more accurate to describe material properties.

To validate the relation for the EMR* it is recommended to manufacture prints for other type of materials and repeat the tensile measurements. If a printing parameter optimization study is performed on this print, it is advised to start at a laser power of 0.061 W and a bed temperature of 164 °C and further increase the laser power from this point. Here, new measurements can still be done for an increasing EMR* and within the limitations due to temperature.

5 Outlook

As shown in Figure 23 warpage considerably limits the range of printing parameters. However, more measurements could be done to find the given limitations of the laser power at a bed temperature of around 164 °C. No measurements were done in this segment of print parameters, as shown in Figure 27, and this could give even more insight on the limitations for print parameters in SLS.

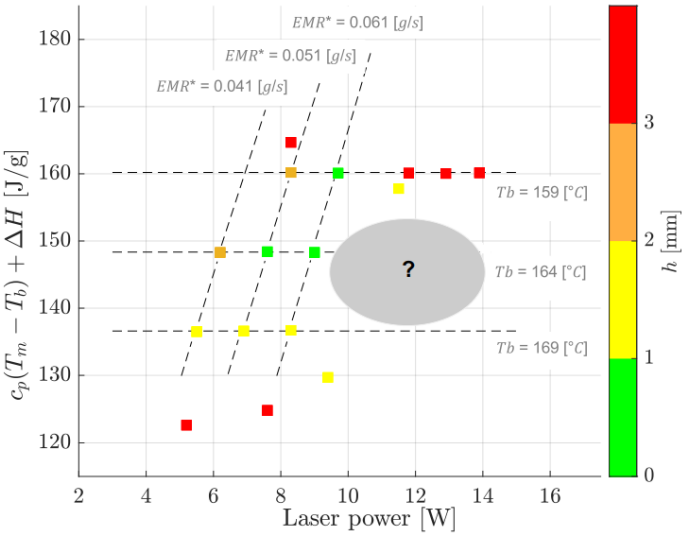

Figure 27: Visualization of area where more measurements can be done within the given limitations for warpage.

Further research on the print parameters in SLS could investigate the relation between the EMR* and material properties for different materials. This could show whether the EMR* is also applicable for other materials. Other materials bring different material characteristics which could influence the accuracy of the EMR* relation. Other materials than PA2200 can be used to prevent postcondensation reactions from impacting material properties. Orgasol for example does not experience the postcondenstaion reactions seen for PA12. Orgasol polyamide powder however does have a higher viscosity, which will require more sintering time to require similar melt [Verbelen et al., 2016].
Next to that, further research can be done for multiple layer prints and prints with a different layer thicknesses. In this study the layer thickness is kept constant. The relation between the addition of the layer thickness to the EMR* and material properties of prints could be studied, since the layer thickness has shown to be an important printing factor in for example the work of [Van Haren, 2022]. Layer to layer interactions should be studied, since adhesion between layers play an important role in part strength in the z-direction. It is possible that hardly no connections are formed between layers. This is a result of the fact that the penetration depth of the laser is not sufficient to sinter the layers together [Van Haren, 2022].
Furthermore, the relation between sintering time and viscosity of the material can be studied, since these have shown to be related [Balemans, 2019]. This could be a good addition to the ETR relation, since the maximum temperature and viscosity have shown to be important factors for mechanical properties [Bierwisch et al., 2021].

References

Balemans, C. (2019). *Computational analysis of polymer powder sintering for 3D printing.* PhD thesis, University of Technology Eindhoven.

Bastiaansen, L. (2019). Exploratory Experimental Study of Multi-Material 3D Food Printing. Master thesis. University of Technology Eindhoven.

Bierwisch, C., Mohseni-Mofidi, S., Dietemann, B., Grünewald, M., Rudloff, J., and Lang, M. (2021). Universal process diagrams for laser sintering of polymers. *Mater. Des.*, 199.

Bourell, D. L., Watt, T. J., Leigh, D. K., and Fulcher, B. (2014). Performance limitations in polymer laser sintering. *Phys. Procedia*, 56(C):147–156.

Drummer, D., Rietzel, D., and Kühnlein, F. (2010). Development of a characterization approach for the sintering behavior of new thermoplastics for selective laser sintering. *Phys. Procedia*, 5:533–542.

EOS GmbH (2019). Material Datasheet PA2200.

Li, J., Yuan, S., Zhu, J., Li, S., and Zhang, W. (2020). Numerical model and experimental validation for laser sinterable semi-crystalline polymer: Shrinkage and warping. *Polymers*, 12(6).

Nelson, J., Vail, N. K., Barlow, J. W., Beaman, J. J., Bourell, D. L., and Marcus, H. L. (1995). Selective Laser Sintering of Polymer-Coated Silicon Carbide Powders. *Ind. Eng. Chem. Res*, 34(5):1641–1651.

Optris (2023). Optris PIX Connect. Retrieved January 18, 2023, from. *https://www.optris.global/optris-pix-connect.*

Plummer, C. J., Zanetto, J. E., Bourban, P. E., and Månson, J. A. (2001). The crystallization kinetics of polyamide-12. *Colloid. Polym. Sci.*, 279(4):312–322.

Schmid, M. (2018). *Laser Sintering with Plastics.* Hanser, Munich, 1 edition.

Schuffenhauer, T., Stichel, T., and Schmidt, M. (2021). Employment of an Extended Double-Integrating-Sphere System to Investigate Thermo-optical Material Properties for Powder Bed Fusion. *Journal of Materials Engineering and Performance*, 30(7):5013–5019.

Starr, T. L., Gornet, T. J., and Usher, J. S. (2011). The effect of process conditions on mechanical properties of laser-sintered nylon. *Rapid Prototyp. J.*, 17(6):418–423.

Van Haren, K. (2022). The effect of surface and volume energy density on part quality in SLS 3D printing. Master thesis. University of Technology Eindhoven.

Vasquez, M., Haworth, B., and Hopkinson, N. (2013). Methods for quantifying the stable sintering region in laser sintered polyamide-12. *Polym. Eng. Sci.*, 53(6):1230–1240.

Verbelen, L., Dadbakhsh, S., Van Den Eynde, M., Kruth, J. P., Goderis, B., and Van Puyvelde, P. (2016). Characterization of polyamide powders for determination of laser sintering processability. *Eur. Polym. J.*, 75:163–174.

ZwickRoell (2023). Tensile Testing Machines and Testers. Retrieved January 18, 2023, from. *https://www.zwickroell.com/products/static-materials-testing-machines/universal-testing-machines-for-static-applications/tensile-tester/.*

Appendix

A.1 DSC measurements

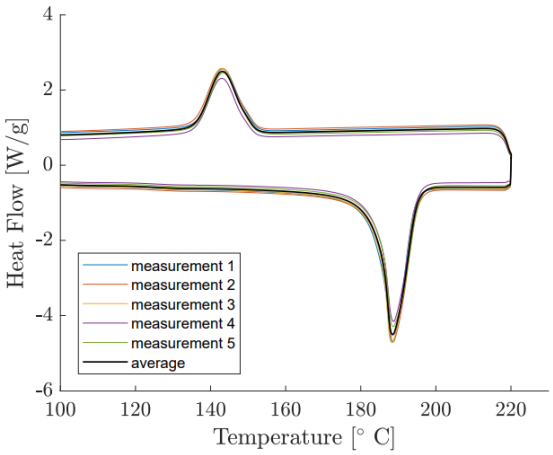

Figure 28: DSC for PA2200 produced in 2022

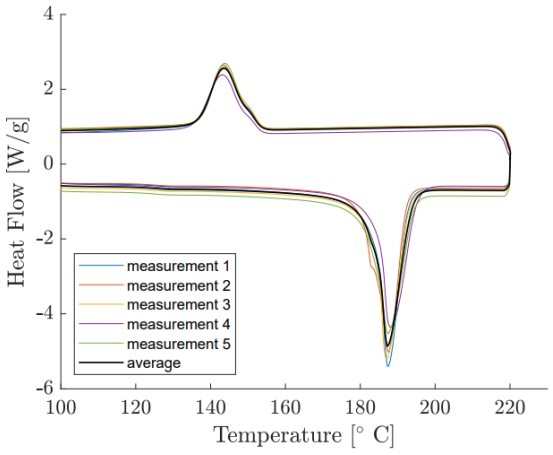

Figure 29: DSC for PA2200 produced in 2018

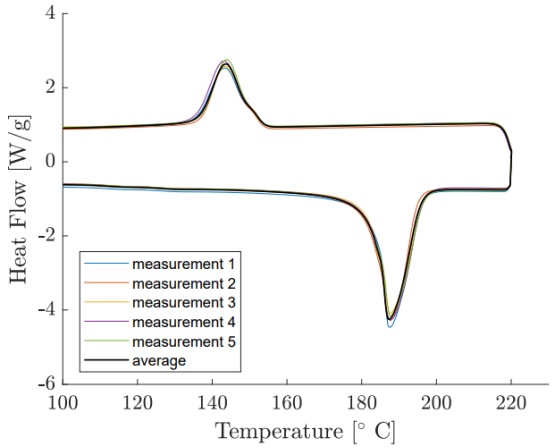

Figure 30: DSC for PA2200 produced by EOS in 2018 conditioned at 100 °C for at least 12 hours.

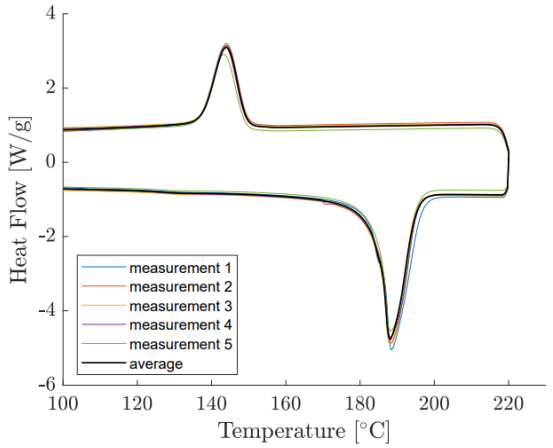

Figure 31: DSC for Duraform produced in 2018

A.2 Successfully printed hexagons

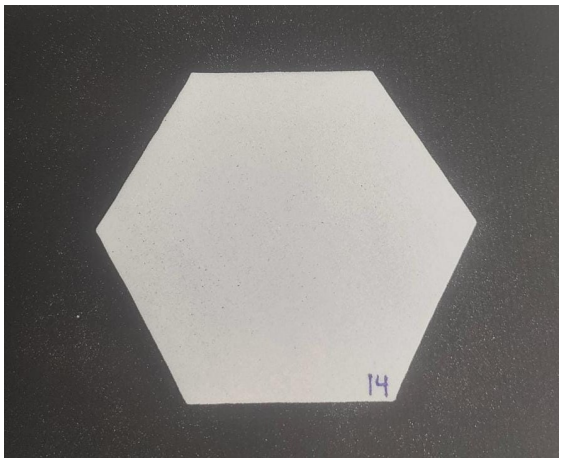

Figure 32: Print 14

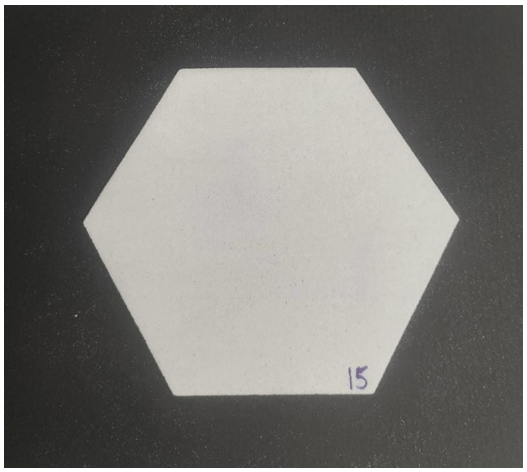

Figure 33: Print 15

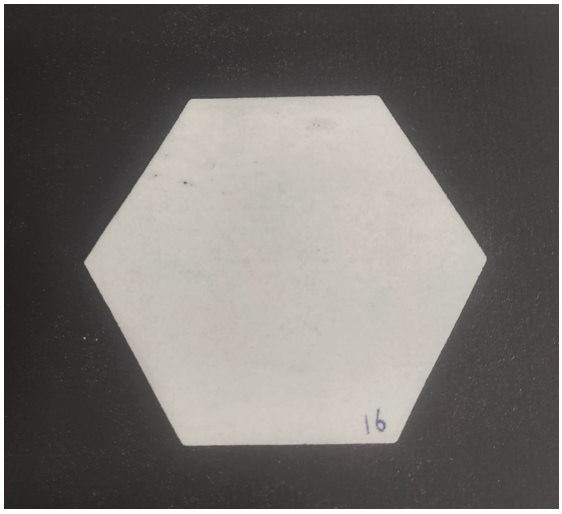

Figure 34: Print 16

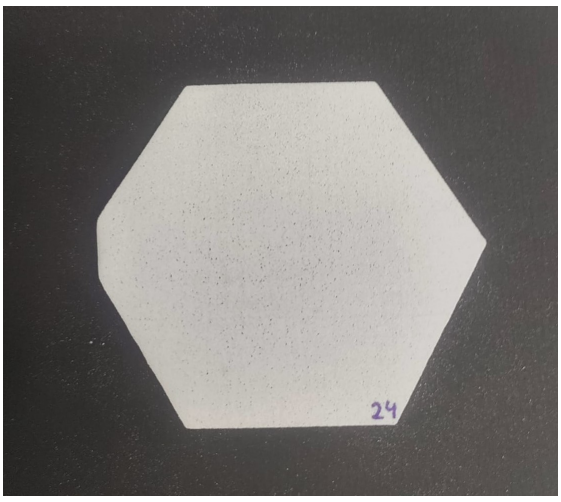

Figure 35: Print 24

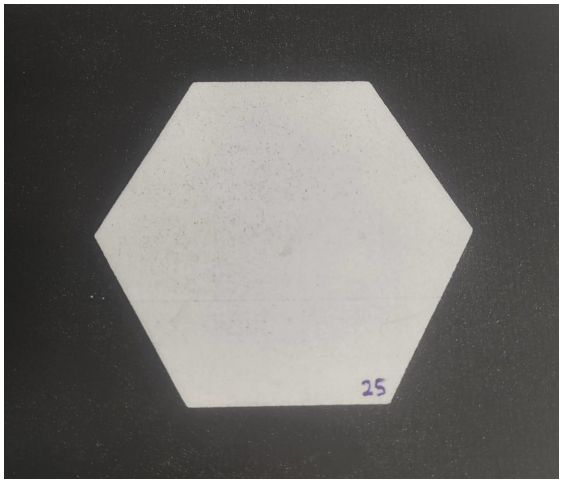

Figure 36: Print 25

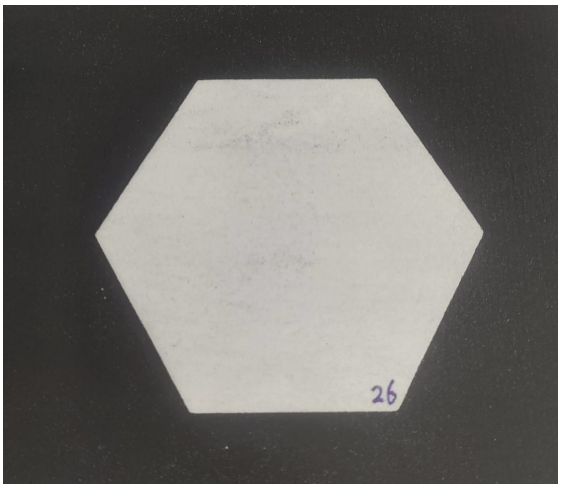

Figure 37: Print 26

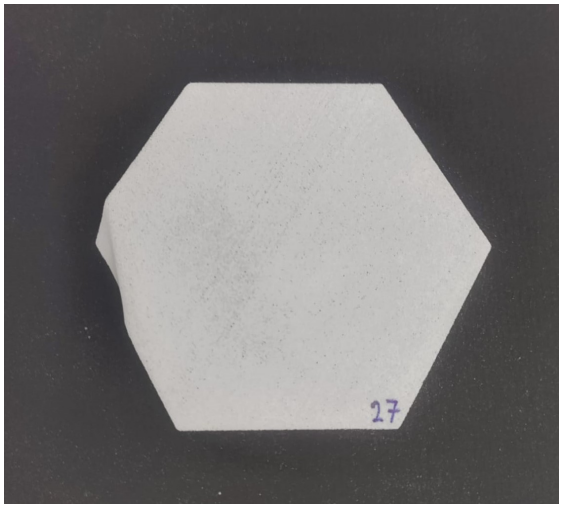

Figure 38: Print 27

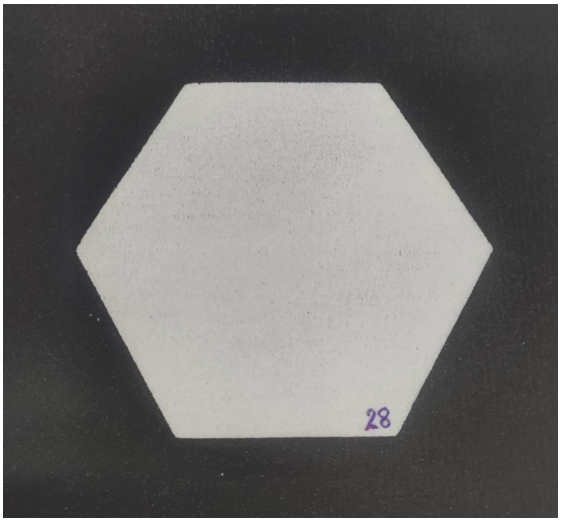

Figure 39: Print 28

A.3 Warpage assessment

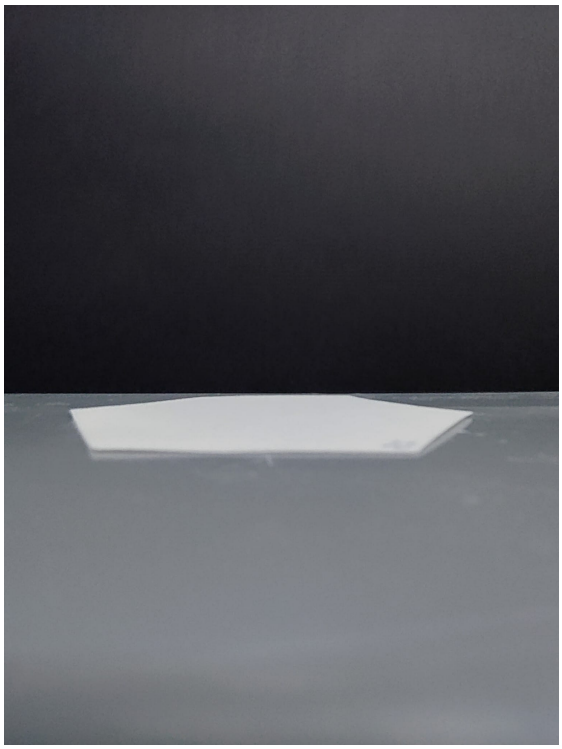

Figure 40: Print 14

Figure 41: Print 15

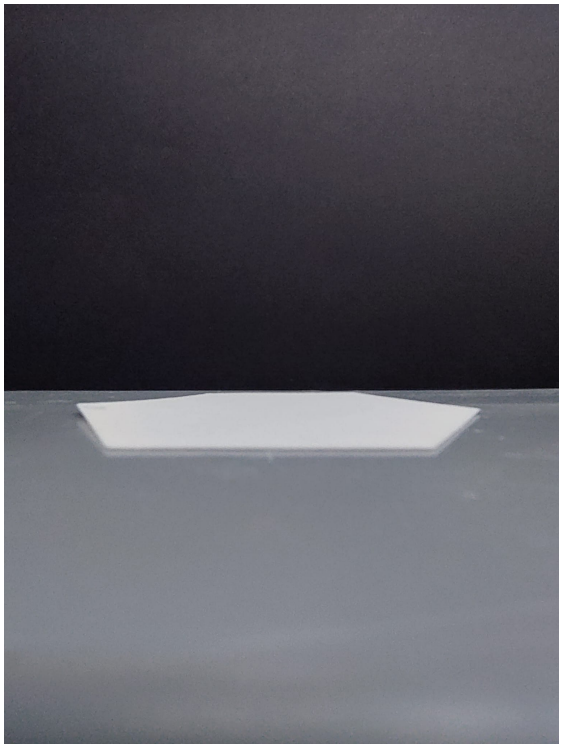

Figure 42: Print 16

Figure 43: Print 24

Figure 44: Print 25

Figure 45: Print 26

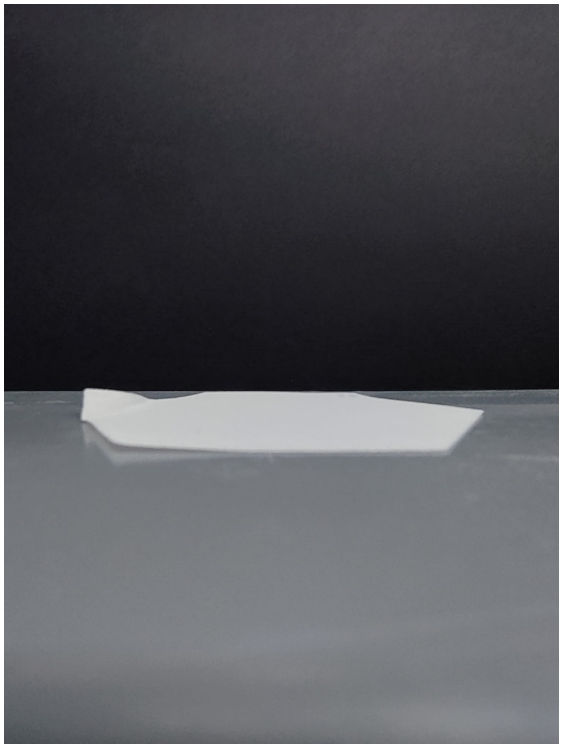

Figure 46: Print 27

Figure 47: Print 28

Figure 48: Print 17

Figure 49: Print 18

A.4 Young's modulus comparison of inside and outside pressed tensile bars

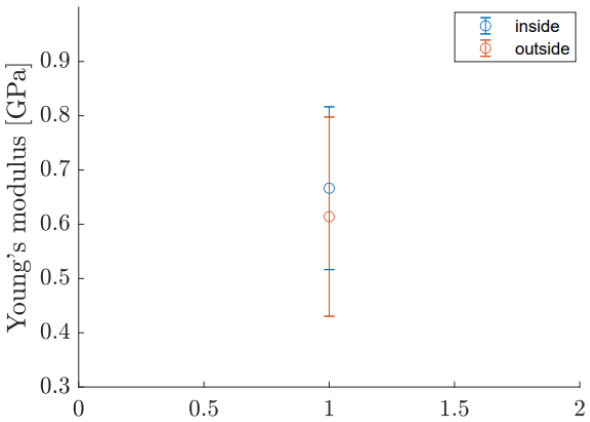

Figure 50: Young's modulus comparison of inside and outside pressed tensile bars